Electronic Supporting Information

Ion Diffusivities in Nanoconfined Interfacial Water Films Contribute to Mineral Carbonation Thresholds

Quin R.S. Miller[a,b]*, John P. Kaszuba[b,c], Sebastien N. Kerisit[a], H. Todd Schaef[a], Mark E. Bowden[d], B. Peter. McGrail[e], and Kevin M. Rosso[a]

[a]Physical and Computational Sciences Directorate, Pacific Northwest National Laboratory, Richland, WA, USA.

[b]Department of Geology and Geophysics, 1000 E. University Avenue, University of Wyoming, Laramie, WY, USA.

[c]School of Energy Resources, 1000 E. University Avenue, University of Wyoming, Laramie, WY, USA.

[d]Environmental Molecular Sciences Laboratory, Pacific Northwest National Laboratory, P. O. Box 999, MS K8-98, Richland, WA, USA.

[e]Energy and Environment Directorate, Pacific Northwest National Laboratory, P. O. Box 999, MS K8-98, Richland, WA, USA.

* Corresponding author contact information: quin.miller@pnnl.gov

Experiment ID[a] T/RH	Temperature (°C)	RH (%)	H_2O solubility in 90 atm $scCO_2$ (mol %)[b]	Reaction time (hrs.)	*in situ* XRD phase abundance (wt %)[c]			TGA-MS carbonate abundance (wt %)[c]	Corrected *in situ* XRD carbonate abundance[d] (wt %)[c]	k (s^{-1}), carbonation rate constant	Uncertainty in k (%)[e]	R^2 of kinetic model fit
					Forsterite Mg_2SiO_4	Magnesite $MgCO_3$	Nesquehonite $MgCO_3 \cdot 3H_2O$					
EXP 1 65/100	65	100	0.608	45.0	13	87	nd[f]	68	67	1.61E-05	10	0.93
EXP 2 65/85	65	85	0.517	44.7	64	36	nd[f]	34	32	2.37E-06	10	>0.99
EXP 3 50/100	50	100	0.378	121.5	nd[f]	99	1	65	73	n/a[g]	n/a[g]	n/a[g]
EXP 4 50/85	50	85	0.321	121.4	100[h]	nd[f, h]	nd[f]	23	NC[i]	5.15E-07[j]	24	0.90[j]
EXP 5 50/85	50	85	0.321	121.5	100[h]	nd[f, h]	nd[f]	23	NC[i]	5.15E-07[j]	24	0.90[j]
EXP 6 50/85	50	85	0.321	45.6	100[h]	nd[f, h]	nd[f]	17	NC[i]	5.15E-07[j]	24	0.90[j]
EXP 7 35/100	35	100	0.367	262.4	2	nd[f]	98	81	81	4.92E-06	10	0.92
EXP 8 35/85	35	85	0.312	171.1	86	nd[f]	14	23	13	1.35E-07	10	0.94

Table S1. Experimental parameters and results for **EXP 1-8**

Abbreviations: $scCO_2$ – supercritical CO_2; XRD - high pressure X-ray diffraction; TGA-MS - thermogravimetric mass spectrometry, RH-relative humidity (% H_2O saturation of $scCO_2$)

[a] Experiments were conducted at 90 atm with 10 µl of H_2O or 4.0 *m* NaCl solution in the reactor fluid reservoir. The *in situ* XRD reactor contained 0.55, 0.75, and 1.55 g of CO_2 at 65, 50, and 35 °C, respectively. Carbon dioxide density at 90 (c.f. Miller et al.[1]), 65, 50, and 35 °C and 90 atm is 178.51, 225.21, 294.77, and 670.24 kg/m^3.[2]

[b] calculated using solubility model of Springer et al.[3]

[c] ±5 wt % uncertainty

[d] Corrected *in situ* XRD abundance accounts for the presence of amorphous silica

[e] At least 10X the uncertainty calculated in SigmaPlot 12.5[1]

[f] not detected

[g] not applicable, due to simultaneous nesquehonite and magnesite growth, the interpolated value is 9.19×10^{-6} s^{-1}.

[h] *in situ* and *ex situ* evidence of magnesite detected, but *in situ* XRD quantification not possible, see text

[i] not calculated, due to lack of *in situ* XRD quantifiable magnesite

[j] k, k uncertainty, and R^2 for 50/85 condition determined using *ex situ* TGA-MS results from EXP 4-6 (see text)

%RH at 50 °C and 90 bar $scCO_2$	Water film thickness (ML)	Water film thickness (nm)
100	5.0	0.92
85	3.6	0.64
70	2.4	0.42

Table S2. Water film thicknesses on forsterite exposed to wet supercritical CO_2 as a function of relative humidity (RH). Water film thickness in monolayers (ML) determined by interpolated/extrapolated measurements from Miller et al.[4], and the water density profile at the (010) forsterite surface derived from the MD simulations of Kerisit et al.[5, 6] were used to determined water film thicknesses in nanometers (nm).

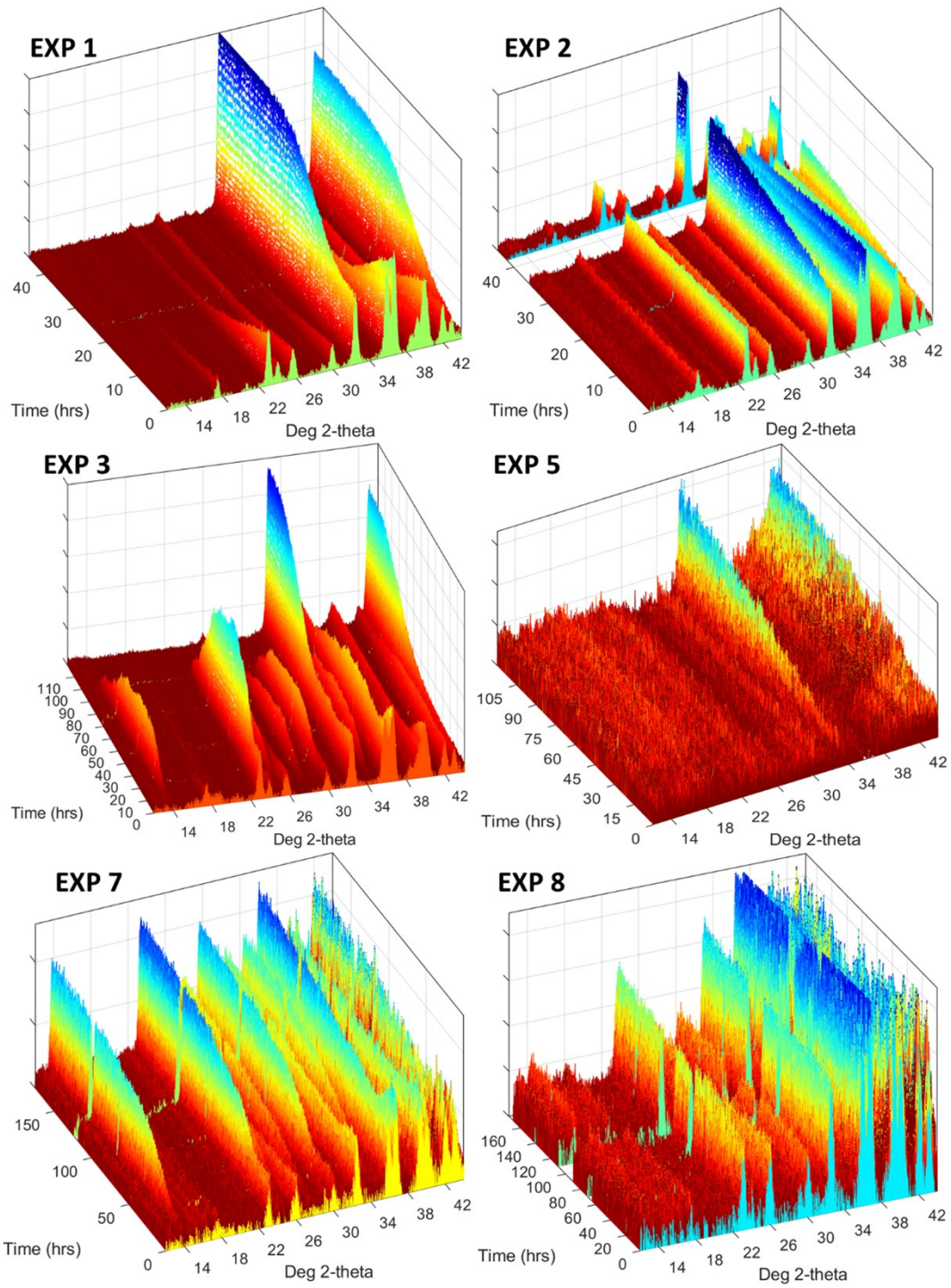

Figure S1. Time-resolved *in situ* diffractograms that show the appearance or disappearance of peaks corresponding to magnesite and/or nesquehonite precipitation and forsterite dissolution at 35-65 °C and 90 atm at 100% and 85% RH. Relative intensity scales are unique to each figure, and cooler colors indicate higher intensities. The EXP 5 plot shows the differential XRD (DXRD) results, in which the initial (t=200 s) *in situ* scan was subtracted from each following pattern to best visualize the growth of magnesite peaks, with only positive intensities shown.

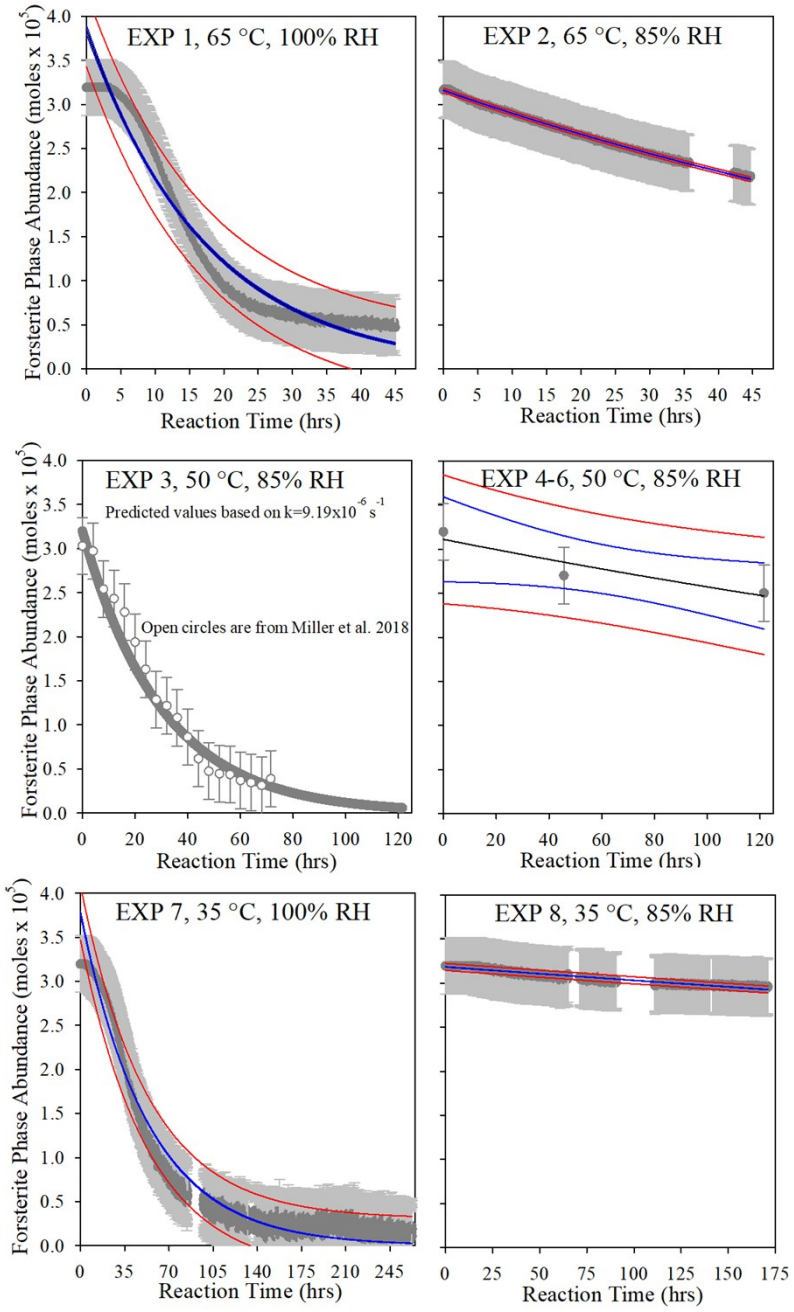

Figure S2. Time-resolved absolute forsterite abundance plots for EXP 1-8 showing Mg_2SiO_4 dissolution at 35-65 °C and 90 atm $scCO_2$ at 100% or 85% RH. Forsterite abundances are denoted by dark grey circles with light grey error bars, and the kinetic model fits (black curve) are shown along with the 95% confidence (blue) and prediction (red) envelopes. The middle left panel (EXP 3) shows a predicted dataset (dark grey curve) of time-resolved forsterite abundances for a rate constant (k) of 9.19×10^{-6} s^{-1}. The rate constant was predicted based on interpolation of the **Fig. 4** Arrhenius plot. For comparison (see text for discussion), data from Miller et al.[7] (open circles) is shown.

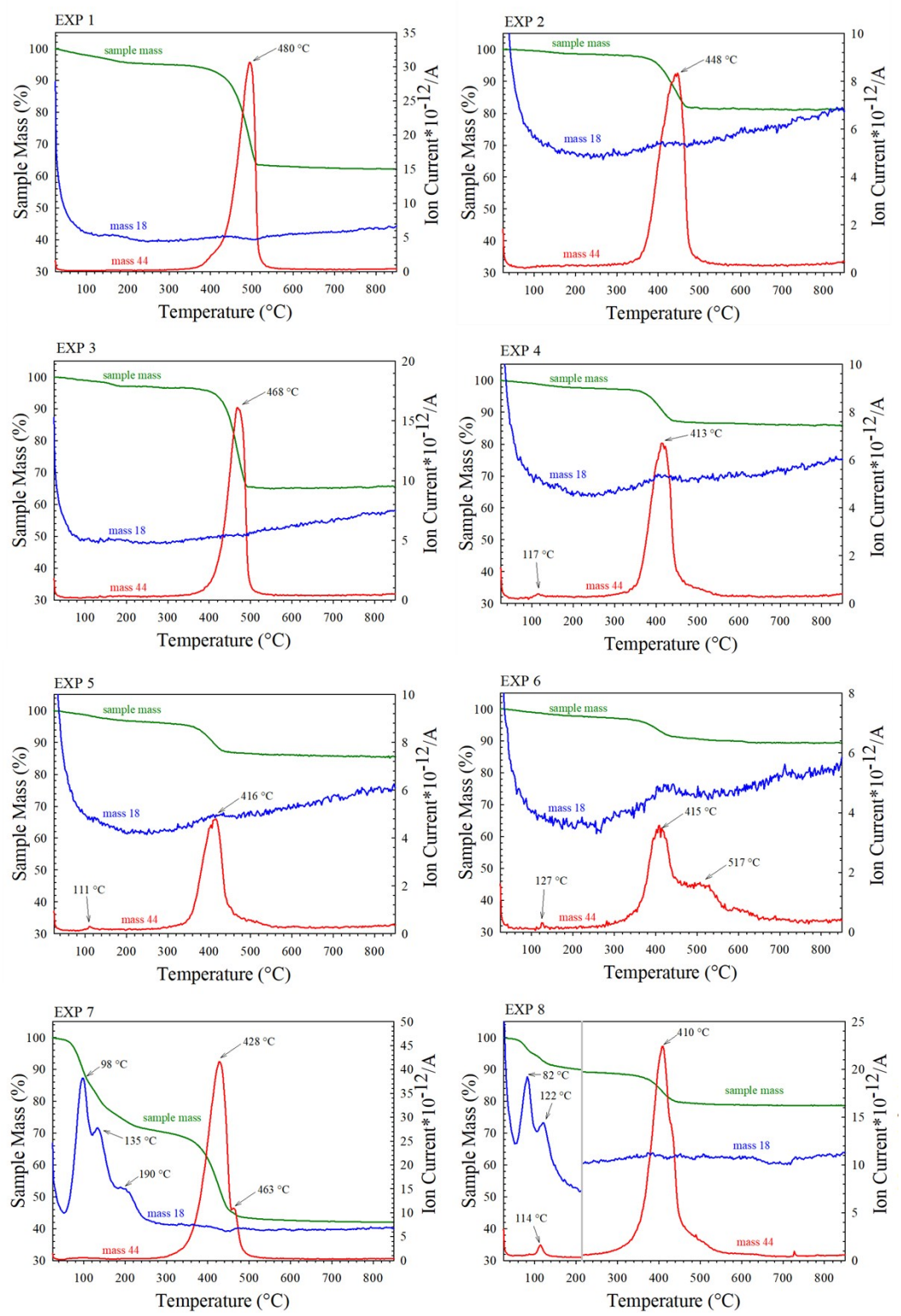

Figure S3. TGA-MS results for EXP 2-8. EXP 1 TGA-MS results reported in Miller et al.[1]. EXP 8 is a composite of two TGA-MS measurements on the same sample, as the first heating ramp was interrupted at ~210 °C.

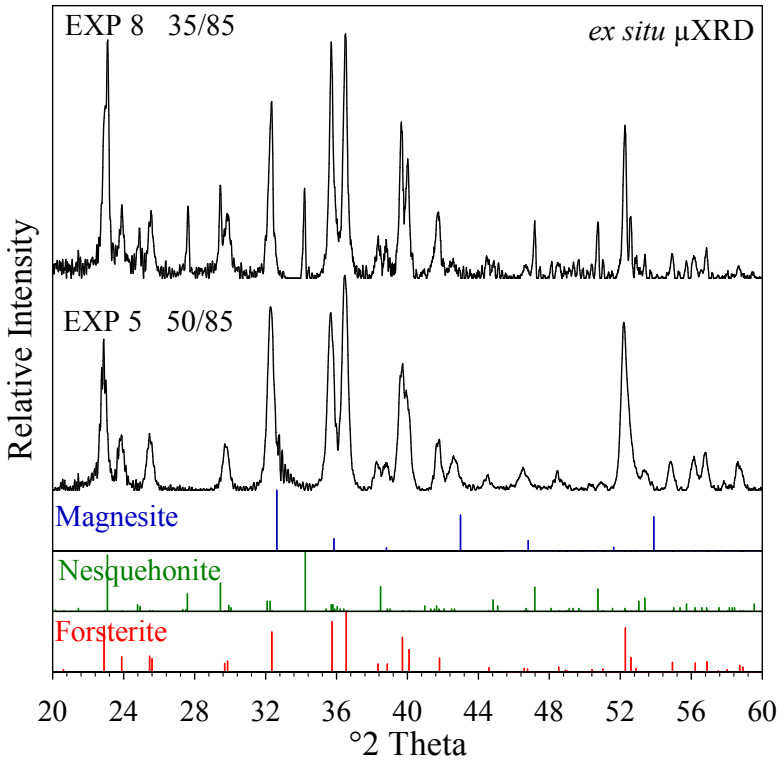

Figure S4. *Ex situ* XRD patterns of EXP 5 and EXP 8. Reference lines in this figure and others correspond to the International Centre for Diffraction Data powder diffraction files (PDF) for forsterite (#34-0189), nesquehonite (#20-0669), and magnesite (#8-0479).

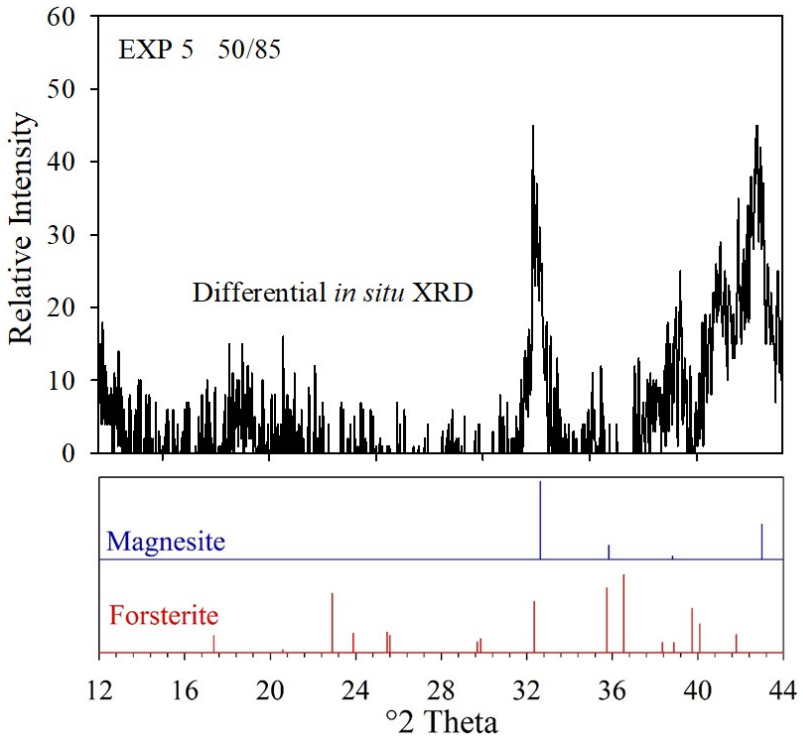

Figure S5. The presence of magnesite peaks is evident in the differential XRD (DXRD) pattern produced by the first and last *in situ* EXP 5 (50/85) diffractograms, with only positive intensities shown.

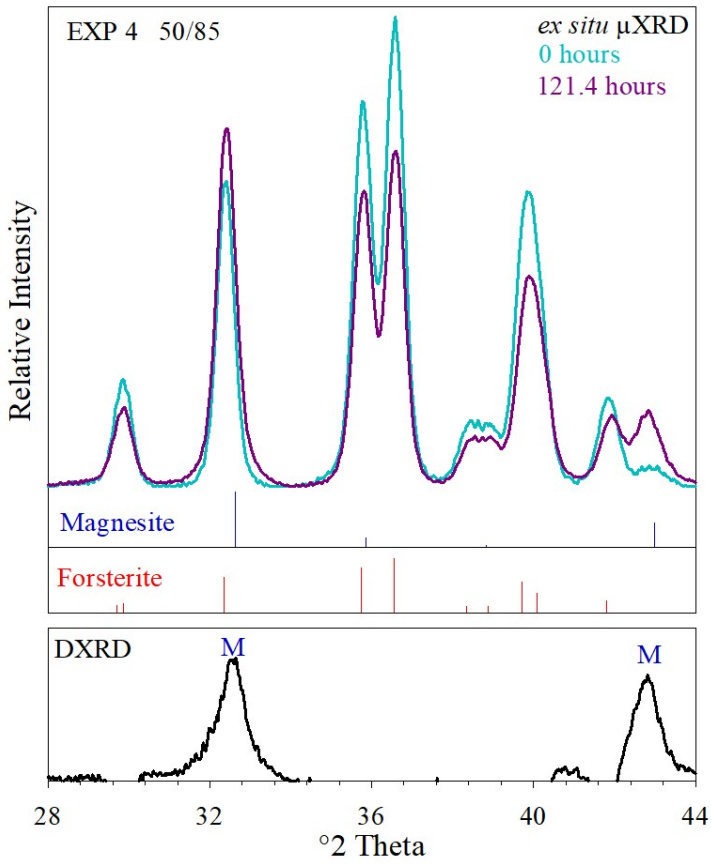

Figure S6. Magnesite (M) peaks are evident in the DXRD pattern produced by the first (cyan) and last (purple) *ex situ* EXP 4 (50/85) diffractograms.

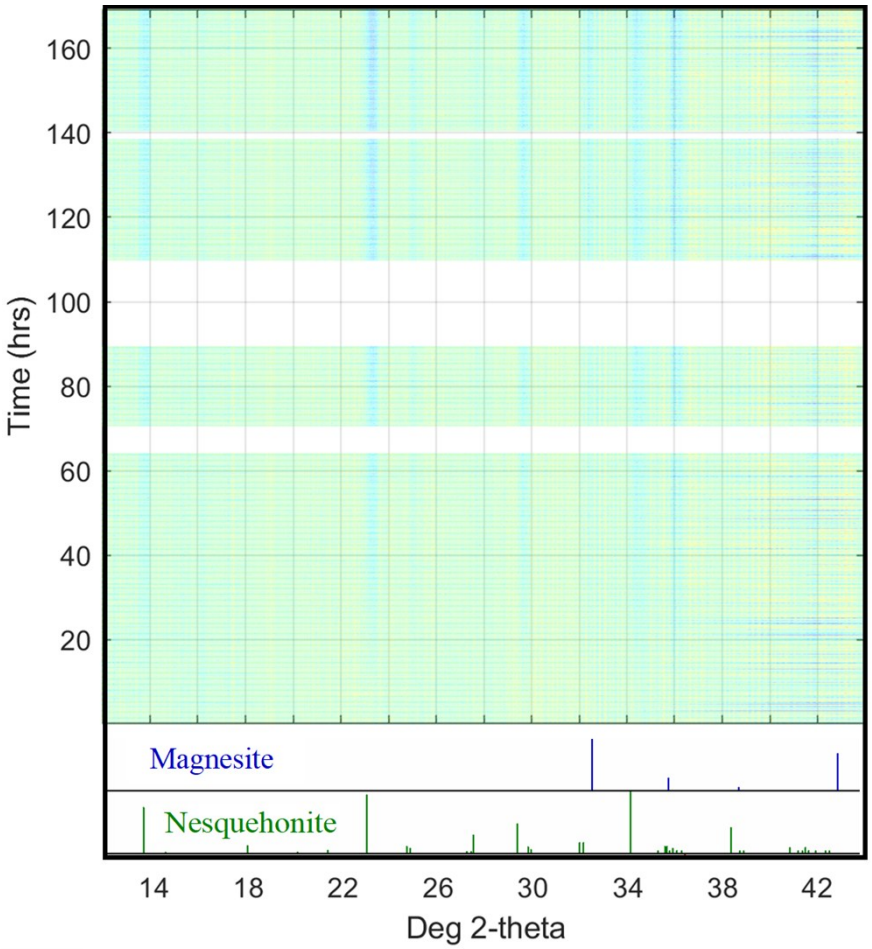

Figure S7. Time-resolved differential XRD results for **EXP 8** (35/85), in which the initial *in situ* scan was subtracted from each following pattern to best visualize the growth of peaks corresponding to nesquehonite. The relative intensities are depicted with an inverse heat scale and the powder diffraction reference files are plotted for clarity.

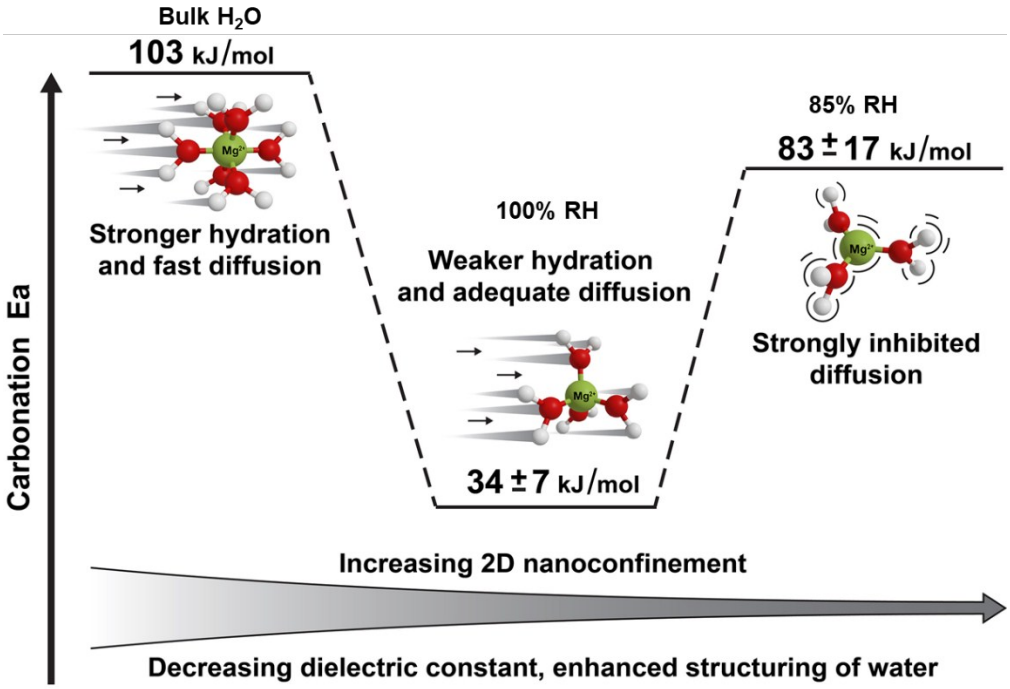

Figure S8. Conceptual illustration of forsterite carbonation "sweet spot" in an interfacial water film due to competing effects between ion hydration and diffusion. See main text (Section 3.3) for discussion.

References

1. Q. R. S. Miller, J. P. Kaszuba, H. T. Schaef, M. E. Bowden, B. P. McGrail and K. M. Rosso, Anomalously low activation energy of nanoconfined $MgCO_3$ precipitation, *Chem. Commun.*, 2019, **55**, 6835-6837.

2. R. Span and W. Wagner, A new equation of state for carbon dioxide covering the fluid region from the triple-point temperature to 1100 K at pressures up to 800 MPa, *J. Phys. Chem. Ref. Data*, 1996, **25**, 1509-1596.

3. R. D. Springer, Z. Wang, A. Anderko, P. Wang and A. R. Felmy, A thermodynamic model for predicting mineral reactivity in supercritical carbon dioxide: I. Phase behavior of carbon dioxide-water-chloride salt systems across the H_2O-rich to the CO_2-rich regions, *Chem. Geol.*, 2012, **322**, 151-171.

4. Q. R. S. Miller, D. A. Dixon, S. D. Burton, E. D. Walter, D. W. Hoyt, A. S. McNeill, J. D. Moon, K. S. Thanthiriwatte, E. S. Ilton, O. Qafoku, C. J. Thompson, H. T. Schaef, K. M. Rosso and J. S. Loring, Surface-catalyzed oxygen exchange during carbonation in nanoscale water films, *J. Phys. Chem. C*, 2019, **120**, 12871-12885.

5. S. Kerisit, J. H. Weare and A. R. Felmy, Structure and dynamics of forsterite-scCO_2/H_2O interfaces as a function of water content, *Geochim. Cosmochim. Acta*, 2012, **84**, 137-151.

6. S. Kerisit, E. J. Bylaska and A. Felmy, Water and carbon dioxide adsorption at olivine surfaces, *Chem. Geol.*, 2013, **359**, 81-89.

7. Q. R. S. Miller, H. T. Schaef, J. P. Kaszuba, L. Qiu, M. E. Bowden and B. P. McGrail, Tunable Manipulation of Mineral Carbonation Kinetics in Nanoscale Water Films via Citrate Additives, *Environmental Science & Technology*, 2018, **52**, 7138-7148.